The Role of Modelling in the Design of Novel Microwave and Millimetre-Wave Reconfigurable Solutions for Global Challenges

A. García-Luque - agl@ic.uma.es - GAAS® Tom Brazil Award Candidature - EuMW Berlin 2023
Telecommunication Research Institute (TELMA), Univ. of Malaga, Bulevar Louis Pasteur 35, 29010 Malaga, Spain

***Abstract* — This candidate contribution aims to outline and highlight the importance of an accurate, efficient and robust modeling of active components as essential factor in the flow process of an engineering project and, specifically, taking into account the novel role of those devices in the design of modern reconfigurable antenna prototypes. These tasks, although attractive, have become a big challenge due to the current RF-paradigm and the demanding operating conditions required in terms of power consumption, frequency and temperature. This two-page abstract introduces a brief summary about the nonlinear modeling tasks relevance and the possibilities of these novel reconfigurable solutions in healthcare, satellite comunications, and wireless technologies together with review of how the proposed EuMIC 2023's accepted paper on equivalent varactor circuits extraction method is useful in this context.**

***Keywords* — Large-Signal mmWave Model, Reconfigurability, Nonquasi-static Circuit, and Nonlinear Vector Network Analyzer.**

I. Introduction & Motivation

It seems that the world has speeded up in recent years as fast as technology evolves. Indeed, the new generation of RF-designs must not only ensure the high-user volume, low consumption, proper signal quality and spectral efficiency demands but, also, do so by garanteeing maximum software and hardware interoperability and integration capabilites. This state-of-the-art *Information Society* predicts that 5G worldwide connections will grow up to nine hundred million by 2023 [1].

In accordance, present-day software advances in artificial intelligence, machine and deep learning are useless without a hardware support infrastructure behind them. Maybe, this is the reason why the design of novel antennas and RF-prototypes adapted to current needs is a hot topic in today's communication industry. A sector where a tradeoff between performance and economic feasibility is compulsory, mainly, for mass manufacturing, i.e., automotive, mobiles, etc. [1].

These new physical developments ought to simultaneously satisfy previous specifications together with latest frequency, power and temperature requirements. At this point, the term "*reconfigurability*" comes into play. A generation of reconfigurable prototypes based on diodes, transistors and varactors [2] are becoming popular in current RF-designs due to their voltage-control capabilities [1], [2]. Thus, not only the power consumption management but, also, linearity control goes through the dominance of the nonlinear behaviour of those active components. In novel antennas, for achieving a reliable and efficient beamforming it is necessary to compensate and understand the nonlinear phenomena associated with those components for high-power injections.

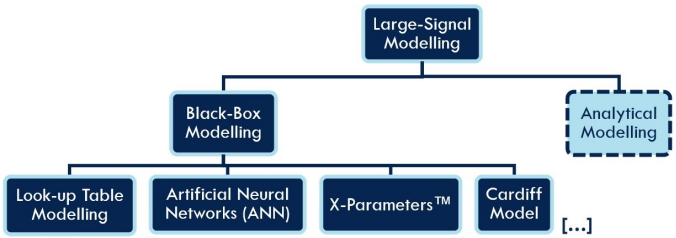

Fig. 1. General overview of today's most popular large-signal modelling techniques splitted into two groups: *Black-Box*-based and *Analytical* proposals.

In this way, it is worthy to spend efforts to the accurate nonlinear characterization of these devices which often exhibit their more remarkable features under large-signal conditions, and to provide affordable models from the extraction view as the SW-compatibility [2]. This idea becomes relevant with the proliferation of AlGaN/GaN, GaAs or SiGe components, the development of novel CAD (Computer Aided Design) tools, and the availability of powerful set-ups, i.e., Nonlinear Vector Network Analyzers (NVNAs). In this challenging frequency and power new paradigm, classical approaches as S-parameters are no longer valid and new solutions are inquired [1].

Even though modelling tasks could seem not as attractive as design, manufacturing or measurement jobs, these are an essencial piece in the engineering project flowchart. In fact, getting accurate models is interesting for reducing optimization efforts and for enhancing more efficient systems from the energy and functional perspectives. Moreover, they will make possible to predict the behaviour of new structures, for example, based on metamaterials, liquid crystals, etc. [1].

A wide range of compact models extraction strategies has been motivated due to the complexity of modern communications circuits. Large-signal modelling techniques are usually divided as in Figure 1. On the one hand, "*Black-Box*" methods are intented to describe the general behaviour without a deep knowledge of the intrinsic plane and just from mathematical functions from DUT's measurements under certain input stimulus. Look-Up Table solutions, Artificial Neural Network proposals, X-Parameters™-based modelling or some specific works as the well-known Cardiff Model, belong to this trend. On the other hand "*Analytical Modelling*" seeks to predict the behaviour by an equivalent circuit whose parameters are constituted from the intrinsic state-functions that characterized the nonlinear response of the device under large-signal conditions. Curtice, Angelov or Tajima models are some famous approached for transistors [1].

II. A Whole New World of Possibilites

A. State-of-the-Art Novel Reconfigurable Applications

The different alternatives listed before have already been successfully proven and validated in different works. All of them, with their advantages and disadvantages, which will be introduced if this proposal is selected for an extended version, are useful for modeling those active devices that have a prominent role in new reconfigurable trends. These exponentially increasing solutions include proposals in which components such as PIN-diodes, varactors or transistors are protagonist. Among them, some of the examples that will be briefly presented on different topics. These drafts are a clear evidence of the wide range of reconfigurable possibilities.

- Firstly, A. Saleeb et al. [3] have recently submitted a technique for the early detection of brain cancer by taking advantage of a circularly polarized reconfigurable antenna array. More concretely, the antenna used was a reconfigurable four-element linear array of squared microstrip patches. Two arrays were designed one circularly polarized, the other linearly polarized, both at Industrial, Scientific and Medical (ISM) 2.4 GHz band. The reconfigurability of the array was achieved using three single pole double throw (SPDT) switches where diodes play a noticiable role. The paper includes some head models considered together with the layout view and a validation based on S_{11} simulated results under several tumor conditions. In this case, a proper model of those PIN diodes is key for a reliable simulated performance versus the experimentation.

- On second place, a newly work of M. Sun et al. [4] introduces a novel multiband frequency-reconfigurable antenna for satellite purposes. This prototype can carry out L-band single frequency operation and S-band dual-frequency operation through electronic tuning. An annular ring and some sawtooth patches are used as radiators for L/S-band operation and excited by a broadband reconfigurable orthogonal network through the coupling of a T-shaped slot and a ring slot in the ground plane, respectively. Therefore, by changing the bias of the PIN diodes loaded on the feed network, the operating frequency can be switched between the navigation and the satellite link receiving state. Thus, the achievement of a highly reconfigurable frequency ratio of a circularly polarized antenna provides solutions for multifunction aperture sharing. The paper shows up several simulated and measured radiation patterns at 1620 MHz (L-band) and 2145 MHz (S-band) operating state, and emphasizes how crucial is the nonlinear PIN diodes modeling for the validation.

- Worlwide interest in satellite communications does not stop growing up currently and it is easy to find more examples of reconfigurable devices in this field. For instance, P. Liu et al. [5] have spent efforts on the design of a novel penta-polarization reconfigurable antenna with mushroom-type metamaterial loading, and operating in x-direction linear polarization (x-LP), y-LP, 45°-LP, left-hand, circular polarization (LHCP) and right-hand (RHCP). For polarization reconfigurability, a dual-port LP mushroom antenna excited by crossed H-shape slot was designed by characteristic mode analysis. Through shifting the states of PIN diodes on the reconfigurable feeding network, the amplitude and phase distributions of two ports of the dual LP antenna were dynamically controlled and the five polarization modes could be achieved. The geometrical reconfigurable feeding network reveals how relevant is the accurate modelling of those PIN diodes in order to predict the device behaviour. C-band surface current distributions and radiation patterns are also presented.

- Otherwise, 5G-mobile communications have become a hot topic nowadays. This is the reason why many studies are working on the optimization of the *5G-New Radio* hardware infraestructure including the development of modern antennas. In this trend, for instance, K. Trzebiatwoski et al. [6] have presented a new 60 GHz-band single-input switched beam antenna for enhancing mmWave 5G automation and integration capabilities. That design is able to electronically switching the main beam in two different directions via a proposed microstrip-line-to-slotline single-pole dual-throw (SPDT) switch based on several PIN diodes. This prototype paves the way for a simple electrical switching mechanism, low-cost manufacturing, and small footprint. All these features make the device ideal for low-cost mmWave 5G-networks. More concretely, details about the required microstrip-to-dual-slotline transition, and the surface current distribution together with the full antenna top-down view and dimensions are described in the paper. The performance is revealed by some radiation patterns (dBi) for some P lengths (with $L1 = 4$ mm), and in the comparison of the simulated and measured beam patterns for both switching states. This antenna is just a small sample of how nonlinear modelling of active devices is essential for enhancing reconfigurability in present-day novel RF-prototypes.

B. EuMIC 2023 Accepted Paper: "Varactor Characterization Procedure for Large-Signal High-Frequency Applications"

At modelling level, solutions are pursued no only in terms of suitable performance, but also straightforward to be integrated into the new CAD tools. Taking advantage of the deep information provided by novel characterization set-ups, i.e., NVNAs, opens up a range of possibilities for designers. An example of an extraction technique proposal which could be useful in these tasks could be the one for varactors to be presented at EuMIC Berlin 2023 [2], and introduced here.

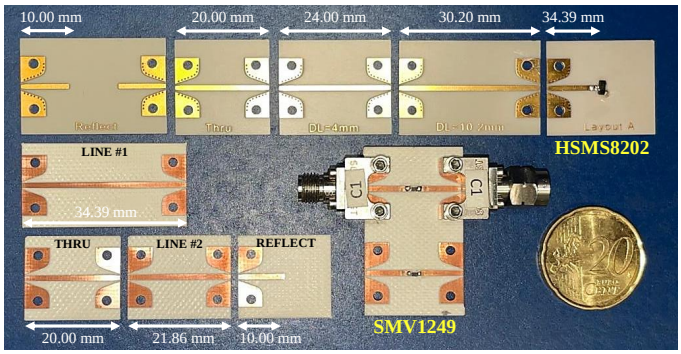

Fig. 2. Microstrip-based access lines and TRL cal-kits layouts for the DUTs.

In particular, that alternative is interesting in three ways: Firstly, because this work introduces a robust extrinsic network extraction process from multi-bias S-parameters, and the direct retrieval of the intrinsic nonlinear state-function from single-tone injection measurements. Secondly, due to the model includes a non-quasi-static (NQS) version which considers the finite time required for the electric charges redistribution when control voltage changes and noticeable at higher frequencies, an useful formulation according to the new specifications of low latency and high bandwidth demands. Lastly, due to the method has been validated with commercial devices under different power, bias and frequency conditions.

The proposed extraction technique intends, therefore, to enhance the development of realiable compact models, to speed up the CAD-tool compatibility of these novel equivalent circuits, and to boost the optimization and co-design task of novel reconfigurable designs [1]. All these features, within the modern RF-paradigm where if active devices play a main role in new tunable prototypes, it is justified to spend efforts to the accurate nonlinear characterization of these components which often manifest their more interesting properties under large-signal conditions. Diode modeling tasks have recently grew up due to their switch and capacitive capabilities [7].

This contribution shows up the experimental validation of the quasi-analytical extraction technique formulated for one-port devices, including a first-order NQS electric charge approach and numerically tested in [2]. Several diode models were built for verifying the extracted delay state-functions over different technologies. The CAD-tool implementation of the equivalent diode model requires both multi-bias S-parameters and large-signal single-tone (f_0) measurements.

Figs.2 show the Skyworks™ SMV1249 varactor, and Avago™ HSMS8202 Schottky diode under test (DUTs), both ready to be measured with the NVNA PNA-X Agilent™ N5247 by several homemade-manufactured access lines. The varactor was tested "in transmission" (one port per terminal), and the Schottky diode with one grounded port in 20-mils microstrip FR4-CIF™ ($\varepsilon_{eff} = 4.3$ & $tan(\delta) = 0.01$), and RO4003C™ ($\varepsilon_{eff} = 2.8$ & $tan(\delta) = 0.002$), respectively.

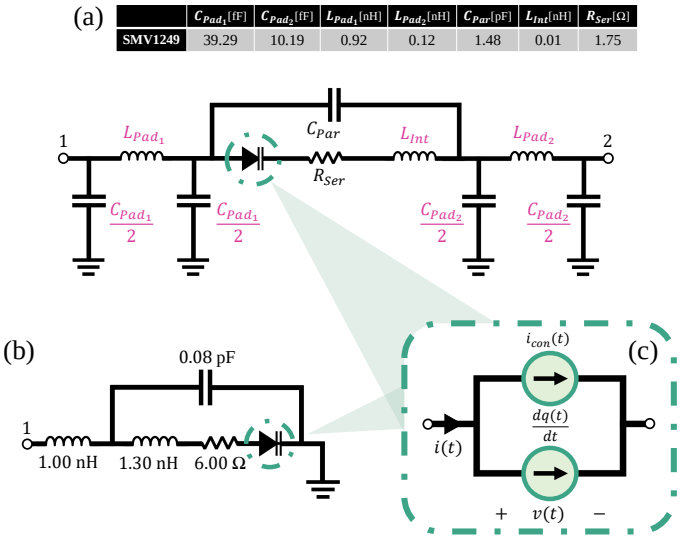

Fig. 3. (a) Proposed equivalent varactor circuit and extracted values. (b) Avago™ HSMS 8202 linear elements. (c) Two-current-based intrinsic model.

1) *Parasitic Network Step-by-Step Estimation*

A generic linear circuit with a π-access equivalent-line was proposed as high-frequency solution for the varactors (Fig. 3.a). For the Schottky diode, datasheet values were considered for the tests (Fig. 3.b). The proposed methodology not only pays attention to the intrinsic nonlinear device (Fig. 3.c), but also presents, as mention, a strategy to characterize the extrinsic linear network for high frequency purposes. The whole extraction flowchart is described in Fig. 4.

That process, which is fully described in the corresponding EuMIC Berlin 2023 paper [2], leads firstly to the extrinsic pad capacitances estimation. For C_{Pad_1}, C_{Pad_2}, and C_{Par}, just reverse DC-points are needed. At low frequencies (e.g., MHz and lower GHz-unit range) extrinsic capacitances are dominant over inductances according with [8].

As a consequence, Fig. 3.a is turned into a low-frequency approach where inductances are negligible. Once the inductances have been removed, if, additionally, a very reverse-bias ($v << V_J$) is applied, it will be assumable that the series resistance R_{Ser} is small enough in comparison with the reverse-biased nonlinear junction resistance $R_j(v)$. Under these conditions, the equivalent Y-parameter matrix [2] allows the analytical extraction of the varactor equivalent pad capacitances C_{Pad_1} and C_{Pad_2} by:

$$C_{Pad_1} = \frac{\Im\mathrm{m}[Y_{11} + Y_{12}]}{\omega} \qquad C_{Pad_2} = \frac{\Im\mathrm{m}[Y_{12} + Y_{22}]}{\omega} \tag{1}$$

Similarly, Y_{12} parameter can be used to compute the total capacitance $C_{Total}(v) = C_j(v) + C_{Par}$ by the curve-fitting of both terms of (2) from the previous Y-matrix [8]:

$$C_{Total}(v) = \frac{\Im\mathrm{m}[-Y_{12}(v)]}{\omega} = \underbrace{C_{j0}\left(1 - \frac{v}{V_J}\right)^{-M}}_{C_j(v)} + C_{Par} \tag{2}$$

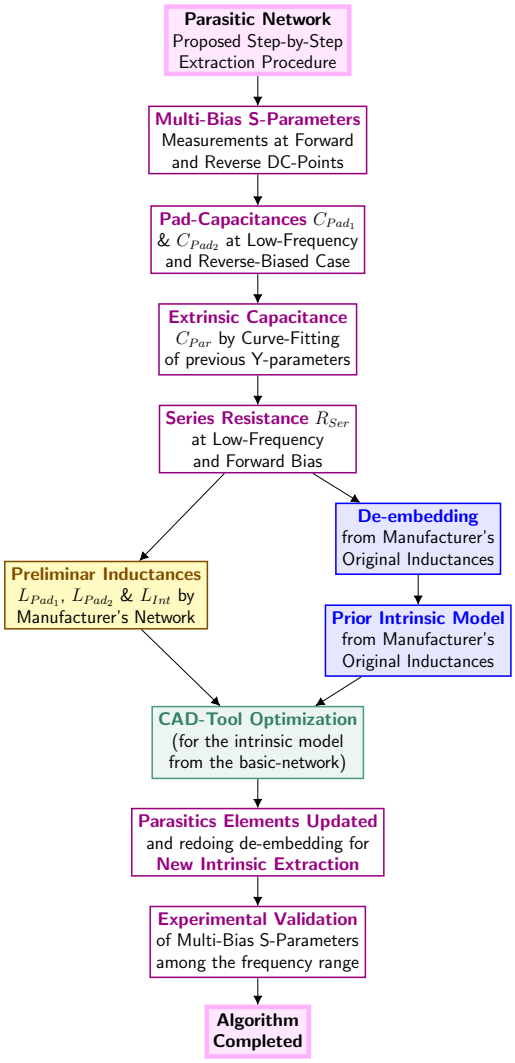

Fig. 4. Step-by-Step extrinsic network parameters extraction flow.

being the right side the common intrinsic varactor capacitance where C_{j0}, M, V_J, and C_{Par} are the unknowns. This curve-fitting is done in MatLab™ where C_{Par} is solved.

2) *Extrinsic Resistance Retrieval*

Secondly, bias-dependence junction resistance $R_j(v)$ is typically prevalent over the almost bias-independent R_{Ser} at reverse-bias, and $C_j(v)$ is negligible at forward-bias [8]. This means that it is possible to estimate R_{Ser} at low-frequency and forward-biased case, where $R_J(v)$ is almost zero. Thus, $R_{Total}(v)$ asymptotically tends to R_{Ser} for positive voltages:

$$R_{Total}(v) = R_{Ser} + R_j(v) \approx \frac{1}{\Re\mathfrak{e}[-Y_{12}(v)]} \tag{3}$$

3) *Extrinsic Inductances Estimation*

From now on just L_{Pad_1}, L_{Pad_2}, and L_{Int} are unknowns. A difference with the use of dummy structures for specific de-embeddings, the iterative estimation at GHz-hundreds range, or taking advantage of resonance phenomena [2], this

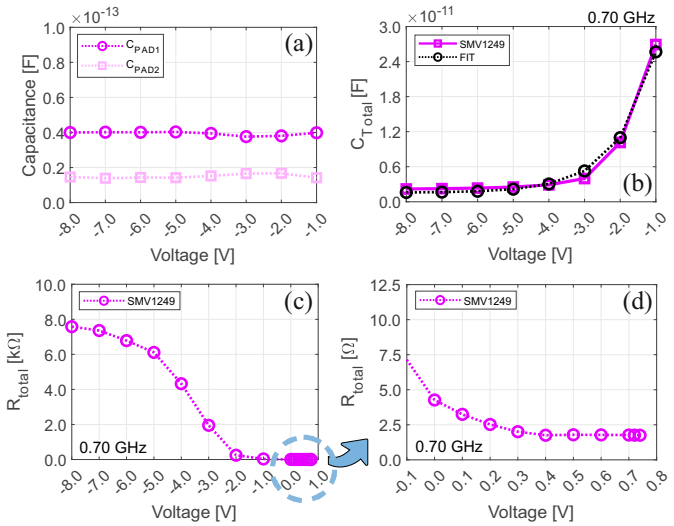

Fig. 5. Extracted extrinsic network for the varactor. (a) Pad capacitances versus bias at 0.7 GHz. (b) Curve-fitting at 0.7 GHz for C_{Par} estimation. (c) R_{Total} at 0.7 GHz including the inset at forward bias in (d) for R_{Ser}.

paper proposes a simpler but equally effective alternative for the computation of the parasitic inductances without a high computational and tedious design cost:

1) The equivalent circuit is built in Keysight-ADS™ from the parasitic capacitances and resistances already extracted together with the original inductances values provided by the manufacturer datasheet as start point. If these ones were no given, nH-orders will be considered analogously with [7] or [8].
2) An analytical de-embedding by Superposition Principle is done for extracting a preliminar intrinsic model.
3) Once the preliminar intrinsic model was computed with the NFS-based method, an ADS™ gradient-optimization is applied (cost function $(|S_{xy}^{model} - S_{xy}^{meas}|)^2/M \approx 0$ for $M = 201$ frequency samples) for all the measured S-parameters. This procedure will upgrade the extrinsic network. The *mean relative error* ($\bar{\delta}$) defines the validation by averaging for $x, y = 1, 2$ ports and M points:

$$\delta_{xy}[\%] = mean|_M \left(\left| \frac{S_{xy}^{model} - S_{xy}^{meas}}{S_{xy}^{meas}} \right| \cdot 100 \right) \tag{4}$$

$$\bar{\delta}[\%] = \frac{(\delta_{11}[\%] + \delta_{12}[\%] + \delta_{21}[\%] + \delta_{22}[\%])}{4} \tag{5}$$

4) Once linear elements were updated, it is feasible to redo a de-embedding for estimating the final intrinsic equivalent model. This methodology is given for the QS and the NQS versions. Matching between measurements and ADS™ S-parameters simulations will certify the goodness of the model. Parasitic elements extracted for the QS and NQS models are in the same order, which gives robustness to the process.

After this iterative sequence, the whole parasitic network is known. The final extracted results for the varactor are included in the Figs. 5 graphs and in Table 1 values [2].

Table 1. Skyworks™ device under test with their parasitics and intrinsic parameters together with the linear network extracted for both varactor models.

Commercial SMV1249		Equivalent Extracted Model		
L_S	0.70 nH	C_{Pad_1}	39.29 fF	41.34 fF
C_P	1.68 pF	C_{Pad_2}	10.19 fF	9.04 fF
R_S	1.70 Ω	C_{Par}	1.48 pF	1.76 pF
I_S	1.00e-14 A	L_{Pad_1}	0.92 nH	0.91 nH
C_{j0}	36.40 pF	L_{Pad_2}	0.12 nH	0.09 nH
M	70.00	L_{Int}	0.01 nH	0.03 nH
V_J	80.00 V	R_{Ser}	1.75 Ω	1.41 Ω
			QS Proposal	NQS Version

4) *Nonlinear Intrinsic QS/NQS Models by NFS Operator*

The intrinsic nonlinear model of the varactor is key for providing a reliable solution for the new generation of high-frequency reconfigurable applications. The idea to compare the experimental performance of a diode QS equivalent circuit versus a NQS intrinsic proposal comes from, as mentioned, the need to design at higher frequencies for satisfying new bandwidth specifications. A first-order NQS electric charge definition, described in [2], is considered to model the finite times required for the redistribution of electric charges from the voltage changes.

A dynamic model of an electron device can be built by a resistive and a capacitive-related current component source per port. In that manner, after a large-signal single-tone (f_0) injection, the commercial device is characterized by a port current $i_{ext}(t)$ and voltage $v_{ext}(t)$. Several de-embedding strategies can be carried out in order to estimate the intrinsic current $i(t)$ and the junction voltage $v(t)$ by removing the linear network (Fig. 3.c). Total $i(t)$ is the analytical sum of a conduction $i_{con}(t)$ and a charge-displacement $i_{dis}(t)$ component representing the resistive nonlinear current and the capacitive phenomena charge source, respectively:

$$i(t) = \underbrace{i_{con}(v)}_{\text{QS}} + i_{dis}(t) \quad \text{where} \quad i_{dis}(t) = \underbrace{\frac{dq(t)}{dt}}_{\text{QS or NQS}} \tag{6}$$

- The electric charge $q(t)$ and, thus, the $i_{dis}(t)$, is the single difference between the QS and NQS models. The resistive part $i_{con}(v)$ is assumed to be a QS magnitude.
- A QS state-function is exclusively dependent of instantaneous changes in the control voltage v. The displacement current $i_{dis}(t)$ comes from a QS or a 1st-order NQS charge depending on the model version.

The Nonlinear Function Sampling (NFS) operator (generic example in Fig. 6) plays a key role in both equivalent circuits. The **quasi-static (QS) model** is formed by a nonlinear QS conduction current $i_{con}(v)$ and a QS electric charge definition $q_{QS}(v)$ whose first derivate is the so-called displacement component, i.e., $i_{dis}(t) = dq_{QS}(v)/dt$ [2]. The method will allow the estimation of the unknown state-functions spectral coefficients I_{con_k} and Q_{QS_k} just from the voltage and current waveforms measured at device ports under a single-tone characterization (f_0) in several steps:

- After a de-embedding, the intrinsic current is defined as:

$$I_k = I_{con_k} + j\omega_k Q_{QS_k} \quad \forall k. \tag{7}$$

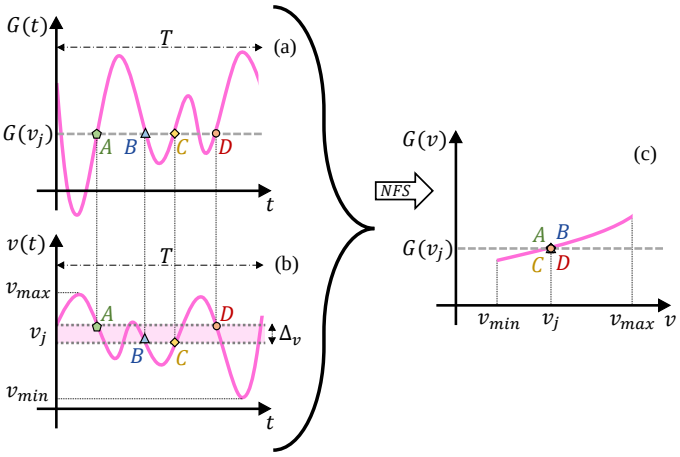

Fig. 6. (a-b) Four samples, i.e. A, B, C and D, of a generic QS-function $G(t)$, which exclusively depends of a control voltage $v(t)$, are turned into a v_j (X axis) and $G(v_j)$ (Y axis) single value in the (c) voltage domain by NFS operator if Δ_v discretization is small enough to belong to a same v interval.

- All involved magnitudes in (7) can be turned into frequency domain by a Fourier Series formalism under a periodic regime ($T = 1/f_0$) for a DC+N harmonics limited bandwidth. For a generic $g(t)$ function:

$$g(t) = \sum_{k=-N}^{N} G_k e^{(j\omega_k t)} = G_0 + \sum_{k\geq 1}^{N} [2\Re\mathfrak{e}[G_k]cos(\omega_k t) - 2\Im\mathfrak{m}[G_k]sin(\omega_k t)] \tag{8}$$

  where $\omega_k = k(2\pi f_0)$, with $k = 0$ [DC], $\pm 1, ..., \pm N$, and G_k are the complex spectral Fourier coefficients.
- Unfortunatelly, this "Current Balance" (7) set of equations is not enough to obtain the unknown I_{con_k} and Q_{QS_k} magnitudes. Here, the NFS operator is key by considering that both state functions are exclusively controlled by the instantaneous junction voltage $v(t)$.
- The NFS operator will map waveforms into the voltage domain as in Fig 6 example. As plotted, for a generic QS function $G(v)$, the control voltage v domain, i.e. D_v (with excursion between v_{min} and v_{max}), is divided into some intervals of equal voltage length Δ_v. If this discretization is small enough, each $G(t)$ sample, corresponding to a v level falling inside a given interval, could be approximated by a unique value v_j and associated with the average voltage $G(v_j)$.
- Thus, it is imposed that all the samples of a QS function which belong to any time instant when $v(t)$ takes a unique value are, indeed, univalued in the voltage-domain, by:
  - Let v_j (for $j = 1, 2, ..., N_v$) be the values of the control voltage v where the N_v samples of the QS-functions will be evaluated.
  - With t_j^p (for $p = 1, 2, ..., P_j$) as each one of the P_j time samples corresponding to $v(t_j^p)$ in the Δ_v interval around the corresponding v_j voltage level.

The formalism leads to this $i_{con}(v)$ definition for each voltage value v_j (analogous for the $q_{QS}(v)$ function):

$$i_{con}(v_j) \approx i_{con}(v(t_j^p)) \approx \frac{1}{P_j}\sum_p i_{con}(v(t_j^p)) \tag{9}$$

After the Fourier Series-based expansion of $i_{con}(v)$ (8) and the application of the NFS operator (9), a proper voltage discretization is required. That means a small enough Δ_v value and, makes possible to assume for each p (as well as for the cos terms):

$$\begin{aligned} &\underbrace{\Delta sin_k(t_j^p)}_{Error} = \underbrace{sin(\omega_k t_j^p)}_{Value} - \underbrace{\langle sin(\omega_k t_j)\rangle_p}_{Average} \approx 0 \\ &\text{where} \quad \langle sin(\omega_k t_j)\rangle_p \equiv \frac{1}{P_j}\sum_p sin(\omega_k t_j^p) \end{aligned} \tag{10}$$

As a consequence, (11) comes from applying the (10) condition to the previous NFS-based equation (9):

$$\begin{aligned} &\sum_{k=1}^{k=N}\left[2\Re\mathfrak{e}[I_{con_k}]cos(\omega_k t_j^p) - 2\Im\mathfrak{m}[I_{con_k}]sin(\omega_k t_j^p)\right] \approx \\ &\sum_{k=1}^{k=N}\left[2\Re\mathfrak{e}[I_{con_k}]\langle cos(\omega_k t_j)\rangle_p - 2\Im\mathfrak{m}[I_{con_k}]\langle sin(\omega_k t_j)\rangle_p\right], \end{aligned} \tag{11}$$

The mathematical process ends by rewriting (11) from the previous approach (similar for Q_{QS_k} coefficients):

$$\sum_{k=1}^{k=N} 2\Re\mathfrak{e}[I_{con_k}]\Delta cos(\omega_k t_j^p) \approx \sum_{k=1}^{k=N} 2\Im\mathfrak{m}[I_{con_k}]\Delta sin(\omega_k t_j^p) \tag{12}$$

By convention, $I_0 = I_{con_0}$ and $Q_0 = 0$ and, therefore, the DC-term is excluded from the previous formalisms.

- Once the formulation is completed, the coefficients I_{con_k} and Q_{QS_k} are involved in a over-determined system of equations, which must fulfill simultaneously:
  - The Current Balance introduced in (7):

$$\begin{aligned} \Re\mathfrak{e}[I_k] &= \Re\mathfrak{e}[I_{con_k}] - \omega_k \Im\mathfrak{m}[Q_{QS_k}] \\ \Im\mathfrak{m}[I_k] &= \Im\mathfrak{m}[I_{con_k}] + \omega_k \Re\mathfrak{e}[Q_{QS_k}] \end{aligned} \tag{13}$$

  - A couple of NFS-based expressions (12) for each sample inside a valid voltage interval ($P_j \geq 2$).

The final overdetermined system of equations can be solved, for instance, by well-known *Least-Squares* algorithms in exclusive terms of Q_{QS_k} by (13). Its resolution leads to the estimation of the unknown Q_{QS_k} and I_{con_k} coefficients. From that moment, these magnitudes are rebuilt in voltage and time domain for the CAD-tool implementation QS-intrinsic circuit.

Otherwise, the extraction step-by-step procedure for the **nonquasi-static (NQS) model** follows up this procedure. It is worthly mentioning that for a proper semiconductor device high-frequency modeling it becomes necessary to consider electron-mobility relaxation times. In accordance, a 1st-order NQS electric electric charge definition is adopted in order to model NQS phenomena [2] for this new circuit:

$$\frac{dq_{NQS}(t)}{dt} = \frac{dq_{QS}(v)}{dt} - \frac{d[\tau_{QS}(v)i_{dis}(t)]}{dt} \tag{14}$$

where integration of (14) allows a $q_{NQS}(t)$ approach:

$$q_{NQS}(t) = q_{QS}(v) - \tau_{QS}(v)\frac{dq_{NQS}(t)}{dt} \tag{15}$$

Expression (15) has the protagonist role in the NQS equivalent intrinsic circuit, where the proposed varactor intrinsic model is characterized by these definitions:

- A total intrinsic current $i(t)$ and a junction voltage $v(t)$. One of the two internal sources of this current is the QS conduction component $i_{con}(v)$ (resistive phenomena).
- The other component, the displacement current $i_{dis}(t)$, is derived from the instantaneous NQS electric charge $q_{NQS}(t)$, which relies on two QS state functions: a delay function $\tau_{QS}(v)$ and a port electric charge $q_{QS}(v)$.

The extraction strategy will allow to model the NQS electric charge $q_{NQS}(t)$ by extracting the its two unknown QS state functions, i.e, $\tau_{QS}(v)$ and $q_{QS}(v)$, from direct current and voltage port measurements under a single-tone (f_0) injection. A prior estimation of I_{con_k} coefficients is compulsory. This previous step can be done, for instance, by low-frequency techniques where NQS phenomena are negligible.

Once the resistive part (I_{con_k}) is known, Q_{NQS_k} can be known from the time and frequency domain Current Balance:

$$\begin{aligned} i(t) = i_{con}(t) + i_{dis_{NQS}}(t) &= i_{con}(v) + \frac{dq_{NQS}(t)}{dt} \\ I_k &= I_{con_k} + j\omega_k Q_{NQS_k} \end{aligned} \tag{16}$$

At this point, the NQS-based technique uses the convolution operator (*) for turning (15) into the frequency:

$$Q_{NQS_k} = Q_{QS_k} - T_{QS_k} * dQ_{NQS_k} \tag{17}$$

where is possible to apply the discrete convolution definition:

$$Q_{NQS_k} = Q_{QS_k} - \underbrace{\sum_{l=-N}^{l=N} T_{QS_l}\cdot dQ_{NQS_{k-l}}}_{T_{QS_k} * dQ_{NQS_k}} \tag{18}$$

The discrete convolution operator (18) together with the condition that coefficients with subscripts l and $-l$ are complex conjugates will allow a first set of of N+1 equations in terms of the $4\cdot(N{+}1)$ unknown spectral coefficients [2]. This first part of the NQS-model extraction algorithm fulfills a similar goal as the QS-version Current Balance (7).

In parallel, the NFS operator applied to the QS unknown magnitudes ($\tau_{QS}(v)$ and $q_{QS}(v)$) will provide some extra equations (similarly for T_{QS_k}) from (9):

$$\sum_{k=1}^{k=N}\left[2\Re\mathfrak{e}[Q_{QS_k}]\Delta cos(\omega_k t_j^p) \text{-} 2\Im\mathfrak{m}[Q_{QS_k}]\Delta sin(\omega_k t_j^p)\right] \approx 0 \tag{19}$$

To sum up, spectral coefficients of QS charge and delay set an over-determined system of equations given by:

- $N+1$ convolution-based equations as analytically presented and formulated in [2].
- A couple of NFS-expressions as (19) for each sample inside a valid voltage interval (if $P_j \geq 2$).

Now both QS and NQS models are ready to be experimentally extracted and tested under single-tone (f_0) injections for the varactor and the Schottky diode cases.

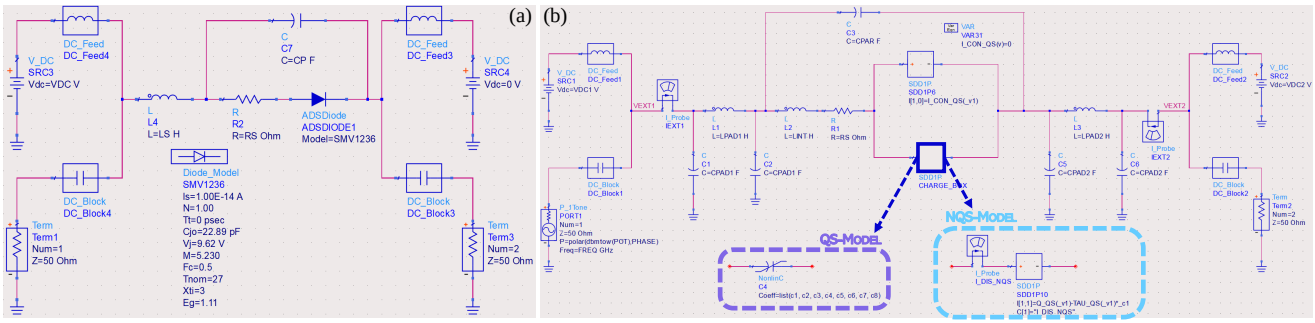

Fig. 7. ADS-Keysight™ HB-Simulations. (a) Foundry, and (b) proposed varactor model with QS (purple) and NQS-circuit (blue) displacement current versions.

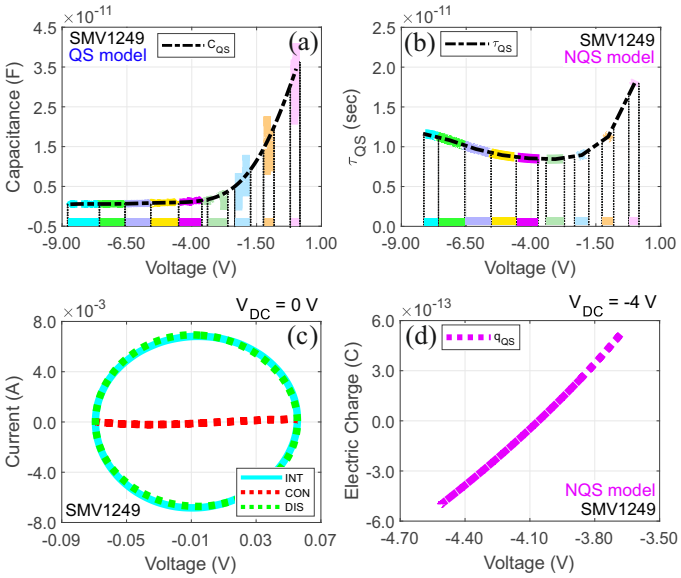

Fig. 8. State-functions for the intrinsic model of the SMV1249 varactor. (a) Fitted capacitance $C_{QS}(v)$ for the QS-model. (b) Extracted delay function $\tau_{QS}(v)$ for the NQS-model. (c) The assumption of $i_{con}(v) \approx 0$ A is valid for varactors. (d) Extracted $q_{QS}(v)$ for the NQS-model at one specific bias.

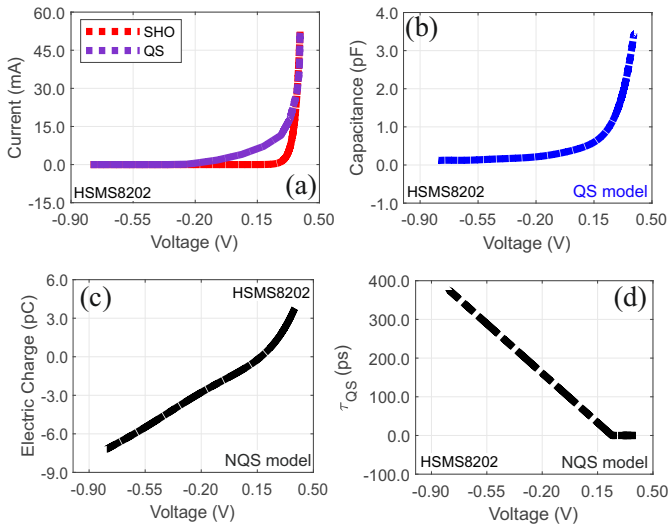

Fig. 9. State-functions for the intrinsic model of the HSMS8202 Schottky diode. (a) Estimated $i_{con}(v)$ QS state function versus Shockley's Law typical approach for the Schottky diode. (b) Fitted $q_{QS}(v)$ for the QS-model. (c-d) Extracted charge $q_{QS}(v)$, and delay function $\tau_{QS}(v)$ for the first-order electric charge approach of the adopted NQS equivalent circuit, respectively.

5) *CAD-Tool Models Implementation*

Foundry, QS and NQS varactor equivalent models were carried out in ADS-Keysight™ where small-signal S-parameters, and Harmonic Balance-based tests were done.

According to Fig.7.a, the Foundry model is built from the manufacturer parasitic network together with the SPICE varactor. The QS and the NQS proposals (Fig.7.b) consider the previous linear network. For the intrinsic plane:

- For the varactor, the resistive part is neglected since these devices commonly operate under negative bias conditions, i.e., both QS and NQS circuits will assume $i_{con}(v) \approx 0$ A. For the Schottky diode, this $i_{con}(v)$ is modeled by the state-function estimated with in the QS model extraction flow.
- For the intrinsic NQS-circuit, the *Symbolically Defined 1-Port Device* (SDD1P) was required for implementing the 1st-order NQS charge recursive expression (15):

$$\underbrace{i[\text{p=1, w=1}]}_{i_{dis}(t)} = q_{QS}(\_v1) - \tau_{QS}(\_v1) * \_c1 \qquad (20)$$
$$C[\text{k=1}] = \text{“}I\_DIS\_NQS\text{”}$$

where the explicit equation (20) defines the displacement current $i_{dis}(t)$ in the p=1 port as the time-domain first-order derivative (i.e. w=1) of the right term $q_{QS}(\_v1) - \tau_{QS}(\_v1) * \_c1$, being $\_v1$ the port voltage, and $\_c1$ the instantaneous current measured by the "I_DIS_NQS" probe. This component is left-placed from the SDD1P block (k=1 port) for (15) recursivity. Moreover, $q_{QS}(v)$ and $\tau_{QS}(v)$ state-functions are curve fitted by several n-order polynomials from the prior MatLab™ extraction according with this generic form:

$$p(v) = p_n \cdot v^n + p_{n-1} \cdot v^{n-1} + ... + p_1 \cdot v + p_0 \qquad (21)$$

- The QS-model replaces the SDD1P block by a nonlinear capacitor for the displacement current component by $C_{QS} = dq_{QS}/dv$ and, also, fitted (21) in both devices.

A deep voltage-discretization (i.e., a small value for Δ_v interval-width) is essential for the (10) condition. This samples-shuffle was performed in MatLab™ by (22) for the j integer (interval-ID) corresponding to a generic v voltage:

$$\Delta_v = \frac{(v_{max} - v_{min})}{N_v} \qquad j = \left\lceil \frac{v - v_{min}}{\Delta_v} \right\rceil \qquad (22)$$

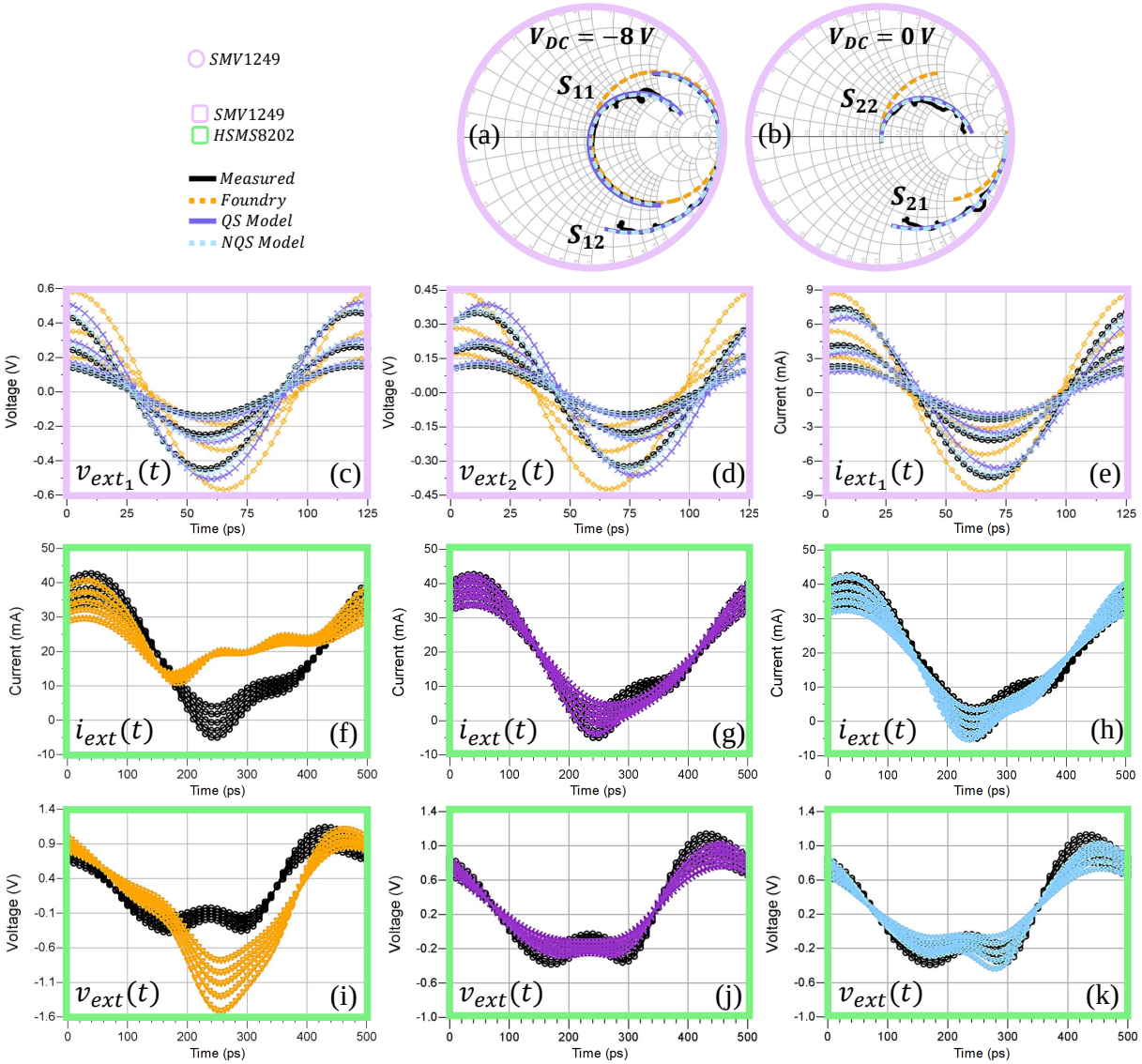

Fig. 10. (a-b) Measured S-parameters (in black) versus Foundry (orange), QS (purple) and NQS equivalent circuits (blue) from 0.7-20 GHz at $V_{DC} = -8$ and 0 V for the SMV1249 varactor (violet). Port voltage and current waveforms under single-tone injection for the (c-e) SMV1249 varactor (violet) at $f_0 = 8$ GHz, $V_{DC} = 0$ V, $P_{RF} = [-5, 0, 5]$ dBm, and the (f-k) HSMS8202 Schottky diode (green) at $f_0 = 2$ GHz, $V_{DC} = 0.27$ V, and $P_{RF} = [9.7 : 1.3 : 15]$ dBm.

where $\lceil\ \rceil$ means rounding to the upper integer, N_v is number of intervals, and v_{max} and v_{min} are the limits of the v intrinsic voltage excursion. The extraction performance was achieved with $N_v = 2{\cdot}10^5$ intervals for $P = 10^4$ time samples, driving into a μV-order interval discretization.

For varactors, it seems that $i_{con}(v) \approx 0$ typical DC IV-assumption is valid for the characterization range. The state functions were estimated just from $f_0 = 1$ GHz data but tested for 1 and 8 GHz waveforms in order to evaluate the response of the varactor equivalent models at higher frequencies where NQS phenomena become noticeable and the frequency extrapolation features of the proposed techniques.

Extracted magnitudes were curve-fitted by (21), and driving into the Figs. 8-9 corresponding to polynomials of 5th-to-7th order, which have been introduced in ADS™ and whose coefficients are not included for extension reasons. These graphs pointed out that the abrupt capacitance-voltage behaviour of the SMV1249 makes it an interesting device for the study of NQS phenomena at higher frequencies [2].

6) *Tests & Experimental Validation*

On the one hand, S-parameters were measured from 0.7 to 20 GHz (with $M = 201$ frequency points) for a reverse $[-8 : 1 : 0]$ V and $[0 : 0.1 : 0.8]$ V ranges. On the other hand, for the intrinsic modeling, the f_0-injection was done with the NVNA PNA-X Agilent™ N5247A at $f_0 = 1$ GHz (for $M = 25$ harmonics), and at $f_0 = 8$ GHz (with $M = 3$) with a power sweep of $[-5 : 0 : 5]$ dBm and a DC-bias range of $[-8 : 1 : 0]$ V for the varactors by involving a piecewise voltage characterization for not exceeding 20 mA limit.

The Schottky diode was measured at $f_0 = 2$ GHz, $M = 5$ harmonics, $P_{ot_{RF}} = [9.7 : 1.3 : 15]$ dBm and $V_{DC} = 0.27$ V. Three dedicated calibrations were needed for a proper single-tone (f_0) acquisition: power, phase and TRL-based.

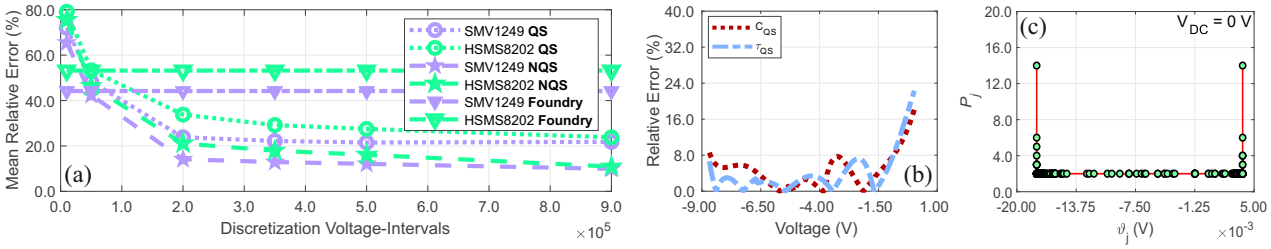

Fig. 11. (a) Mean relative error (%) in experimental waveforms versus some N_v of the extracted-models (b) Error in the QS-model $C_{Q_S}(v)$ state-function, and in the $\tau_{Q_S}(v)$ magnitude of the NQS-model when N_v is not high enough. (c) Number of samples per interval for SMV1249 NQS-model extraction process.

Table 2. Varactor's waveforms performance by mean relative error ($\bar{\delta}$).

Large-Signal Study / Current & Voltage Waveforms				
Bias-Point	$\mathbf{V_{DC} = -8}$ **V**		$\mathbf{V_{DC} = 0}$ **V**	
Injection (f_0)	**1 GHz**	**8 GHz**	**1 GHz**	**8 GHz**
	SMV1249			
Foundry	44.1%	49.8%	46.9%	47.2%
QS Model	5.6%	16.9%	6.5%	18.8%
NQS Model	4.1%	8.5%	5.3%	7.9%

The proposed circuits were validated for:

- 0.70 to 20 GHz S-parameters at $V_{DC} = -8$, 0 and 0.74 V bias for all available models and devices.
- For varactors: Port current and voltage waveforms at $f_0 = 1$ ($M = 25$) and 8 GHz ($M = 3$) for $V_{DC} = -8$ and 0 V DC-conditions, and a power sweep of $P_{ot_{RF}} = [-5, 0, 5]$ dBm. Extractions done at 1 GHz and 5 dBm.
- For Schottky diode: Port current and voltage waveforms at $f_0 = 2$ and 8 GHz for $V_{DC} = 0.27$ V, and a power sweep of $P_{ot_{RF}} = [9.7, 1.3, 15]$ dBm. Extractions done just from 2 GHz ($M = 10$) and 15 dBm in this case.

According with Fig. 10 and Table 2, some conclusions are:

- Multi-bias S-parameters performance of equivalent built-up models is certainly better than the foundry proposal, only valid for few-GHz range. A wider bandwidth frequency response is achieved for all DUTs.
- Waveforms highlight two ideas. Firstly, foundry model is notably improved by the two proposal made. Secondly, it seems that the NQS version is the best alternative when going up in frequency. Indeed, 1 GHz-performance of QS and NQS model simulations are quite similar, but, at 8 GHz, the mean relative error of the NQS version reasonably improves the experimental results.
- The frequency response of the equivalent circuits is good enough for approximate the varactor waveforms at 8 GHz just from the single modeling at 1 GHz. This show up the frequency extrapolation features of the circuits when NQS phenomena seem noticeable (e.g. Table 2).

7) *Voltage-Interval Discretization Review*

A tradeoff between extraction simulation time ($t_{1\text{ GHz}}$) and waveforms performance is presented in Fig. 11.a for the Skyworks™ SMV1249 and an Intel™ i7 6500U 2.5 GHz, DDR4-8GB, and MatLab™ R2022b setup. It is appreciable how the proper behaviour of the extracted circuits relies on the number of selected intervals N_v, which is inversely proportional to Δ_v (22). A high value of N_v means a small Δ_v and leads to a successful extraction. Both QS/NQS solutions offer good overall performance for $N_v \gtrsim 0.5 \cdot 10^5$ intervals. It is also verified how the error is quite similar with both QS and NQS circuits at 1 GHz, but different for 8 GHz waveforms.

The discretization reaches a value where it can no longer improve the achieved error when N_v is high enough (Fig. 11.b). A proper balance between computational time and performance is $N_v = 2 \cdot 10^5$ intervals (Fig. 11.c), and this is why all extraction presented here has been set to that value.

III. Outline & Conclusions

This Tom Brazil Award 2023 candidature pursues to point out the present-day nonlinear modelling tasks as key factor in the development of novel reconfigurable antennas for satellites, healthcare, and communications by requiring the integration of active devices and their proper modelling in order to predict the experimental behaviour and enhance the industrial development workflow. The final-pitch speech will be focus on these modern reconfigurable ideas, different present-day modeling strategies, and how this novel NFS-based extraction technique [2] is useful as large-signal high-frequency solution[1].

References

[1] M. Stettler et al., "Industrial TCAD: Modeling Atoms to Chips," *IEEE Trans. Electron Devices*, vol. 68, no. 11, pp. 5350–5357, 2021.

[2] A. García-Luque et al., "Varactor Characterization Procedure for Large-Signal High-Frequency Applications," in *18th European Microwave Integrated Circuits Conference (EuMIC)*, 2023.

[3] D. A. Saleeb et al., "A Technique for the Early Detection of Brain Cancer Using Circularly Polarized Reconfigurable Antenna Array," *IEEE Access*, vol. 9, pp. 133 786–133 794, 2021.

[4] M. Sun et al., "L/S Multiband Reconfigurable Satellite Antenna," *IEEE Antennas Wirel. Propag. Lett.*, vol. 18, no. 12, pp. 2617–2621, 2019.

[5] P. Liu et al., "Broadband & Low-Profile Penta-Polarization Reconfigurable Metamaterial Antenna," *IEEE Access*, vol. 8, pp. 21 823–21 831, 2020.

[6] K. Trzebiatowski et al., "60 GHz Switched Antenna for 5G-mmWaves," *IEEE Antennas Wirel. Propag. Lett.*, vol. 20, no. 1, pp. 38–42, 2021.

[7] R. Amirpour et al., "Large-Signal Modeling of a Scalable High-Q AlGaN/GaN High Electron-Mobility Varactor," *IEEE Transactions on Microwave Theory and Techniques*, vol. 67, no. 3, 2019.

[8] A. Y. Tang et al., "Analytical Extraction of a Schottky Diode Model From Broadband S-Parameters," *IEEE Transactions on Microwave Theory and Techniques*, vol. 61, no. 5, 2013.